Meteorological Variability and the Annual Surface Pressure Cycle on Mars

FRÉDÉRIC HOURDIN, PHU LE VAN, FRANÇOIS FORGET, AND OLIVIER TALAGRAND

Laboratoire de Météorologie Dynamique du CNRS, Ecole Normale Supérieure, Paris, France

(Manuscript received 17 September 1992, in final form 22 March 1993)

ABSTRACT

It is commonly admitted that the seasonal surface pressure cycle, observed on Mars by the two Viking landers, is due to condensation and sublimation of the atmospheric carbon dioxide in the polar caps. A three Martian year numerical simulation has been performed with a Martian General Circulation Model developed from the terrestrial model of the Laboratoire de Météorologie Dynamique. The conditions of the simulation were those of a typical clear-sky situation. The results, validated by comparison to Viking pressure measurements and to temperature fields retrieved from *Mariner-9* measurements, show that the pressure cycle depends on the location on the planet. They strongly suggest that, in addition to condensation and sublimation of the atmospheric carbon dioxide, two other effects significantly contribute to the pressure cycle: an orographic effect resulting from the difference in mean height between the two hemispheres, and a dynamical effect resulting from the geostrophic balance between the mass and wind field. In high latitudes, the pressure variation linked to the dynamical effect may have the same magnitude (about 25%) as the global mass variation due to the condensation–sublimation cycle. A shorter dust storm simulation is also in good agreement with observations, in particular as concerns the surface pressure variations and the low-level winds, independently estimated from observations of the bright streaks on the surface of the planet. These results show that the atmospheric mass budget cannot be correctly estimated from local measurements such as Viking measurements.

1. Introduction

Following the space missions of the 1970s, especially the *Mariner-9* and Viking missions, the atmospheric circulation of Mars has become the best known after that of Earth (e.g., see Leovy 1979; Zurek et al. 1992). This is partly due to the strong similarity between the two planets. On both planets, a large fraction of the incoming solar radiation reaches the surface and both atmospheres are consequently strongly heated by absorption of thermal radiation reemitted by the surface. For both planets, also, the latitudinal energy redistribution is dominated by Hadley circulation in low latitudes and baroclinic waves for the winter midlatitudes. Baroclinic waves are responsible for the short period (between 2 and 5 days) pressure fluctuations visible on the data recorded in situ by the two Viking landers (VL) over more than three Martian years at two points of the Northern Hemisphere (*VL1* at 22.5°N and *VL2* at 48°N). Those pressure measurements are reproduced in Fig. 1. The Martian atmosphere is the site of other remarkable phenomena. Among them is the occasional occurrence of global dust storms, during which the whole atmosphere becomes opaque for the incoming solar radiation, strongly affecting the global atmospheric circulation. The so-called 1977-B dust storm, for example, is responsible for the difference visible in Fig. 1 between year 1 and years 2 and 3 during northern winter ($L_S \sim 275°$ to $L_S \sim 340°$).[1] During this time, both baroclinic waves and the mean pressure were strongly modified at *VL2*. Years 2 and 3, during which no dust storm occurred, are generally referred to as clear years even though the atmospheric dust content still remained significant, with optical depths in the visible range larger than 0.3 at both landing sites.

Another remarkable phenomenon is the seasonal condensation of a significant part of the atmosphere in the polar caps, because of the very low polar night temperatures, which allow condensation of carbon dioxide, the principal atmospheric constituent. This phenomenon, predicted since 1966 (Leighton and Murray 1966), has been widely agreed (Hess et al. 1979; Hess et al. 1980) to be responsible for the large-amplitude, low-frequency fluctuations of the Viking pressure measurements (Fig. 1). The first deep minimum of pressure, near sol 100, occurs during southern winter when a great part of the atmosphere is trapped in the south polar cap (sols are Martian days, sol 0 corresponding to the landing of the first Viking probe). The secondary minimum near sol 430 corresponds to the northern winter, much shorter and less cold than the southern winter because of the high eccentricity of

Corresponding author address: Dr. Frederic Hourdin, Laboratoire de Meteorologie Dynamique du CNRS, Ecole Normale Superieure, 75 231 Paris Cedex 05, France.

[1] L_S is the longitude of the sun in Mars centered coordinates (areocentric longitudes). It is used as seasonal index with $L_S = 0$ at northern vernal equinox.

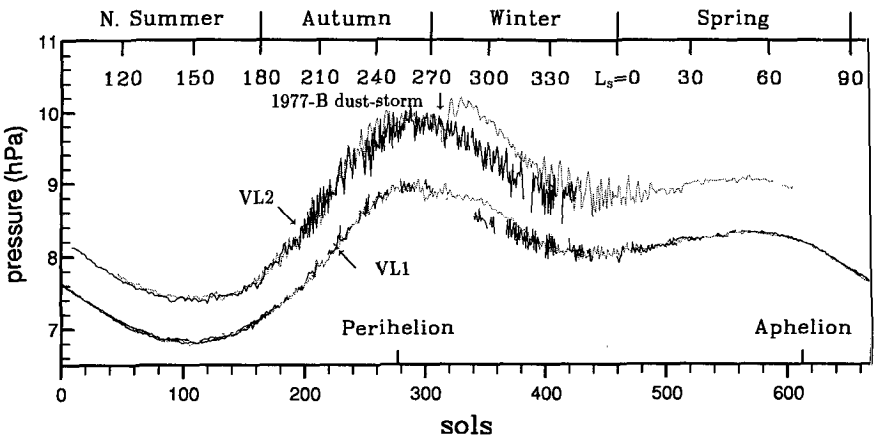

FIG. 1. Time evolution of the surface pressure recorded by the two Viking landers during the first three Martian years of the mission for year: 1 (dotted), 2 (solid), and 3 (dashed) are superimposed on the same graph. Data from Tillman and Guest (1987) (see also Tillman 1989).

the Martian orbit. The picture is not so simple, in fact, because sublimation in one cap and condensation in the other one can occur simultaneously. Nevertheless, the pressure signal at *Viking Lander 1* has been generally considered as representative of the global mass of the Martian atmosphere although some discrepancy appears when trying to superimpose *VL1* and *VL2* results, even after an hydrostatic scaling has been performed in order to take into account the different heights of the two landing sites (Hess et al. 1979).

We report here on the high variability of the annual pressure cycle with the location on the planet. This work is based on numerical results obtained with a new general circulation model of the Martian atmosphere developed in the last three years at Laboratoire de Météorologie Dynamique. The spatial variability is the consequence of two effects: the first, linked to the strong Martian orography, has already been put forward (Hess et al. 1979) to explain part of the discrepancy between the data from the two landers; a second purely dynamical effect due to the geostrophic balance between the pressure field and the strong Martian winds is shown to be of an equivalent strength, at least in high latitudes. This latter effect was described for the first time by Talagrand et al. (1991) and has since been confirmed by Pollack et al. (1993). It had never been put forward before for Mars, whereas it is known that, on Earth, geostrophic balance is responsible for a significant latitudinal pressure gradient in winter high latitudes, especially in the Southern Hemisphere. One consequence of this combined effect is that the annual cycle of the mean atmospheric pressure (or global atmospheric mass) is significantly different from Viking observations. For example, the two pressure maxima, corresponding to minimum of condensation in the polar caps, are shown to be much more symmetric in the planetary mean.

2. The model

The Martian atmospheric general circulation model (GCM) has been adapted from the terrestrial climate GCM of the Laboratoire de Météorologie Dynamique (LMD) (e.g., see Sadourny and Laval 1984). In its Martian version, it is fast enough to perform series of simulations over more than one Martian year, either in a low-resolution version on a workstation or in an higher resolution on a CRAY-2. It must be emphasized that it is the first GCM to be fully integrated over more than one Martian year. A brief description of the model is given below.

a. Dynamics

The dynamics are directly taken from the LMD terrestrial GCM. They are based on a finite-difference formulation of the classical primitive equations of meteorology, which are a simplified version of the general equations of hydrodynamics based on three main approximations: 1) the atmosphere is assumed to be a perfect gas, 2) it is supposed to remain vertically in hydrostatic equilibrium, and 3) the vertical dimension of the atmosphere is supposed to be much smaller than the radius of the planet (thin-layer approximation). In the original formulation (Sadourny and Laval 1984), the potential enstrophy was numerically conserved for barotropic flows (Sadourny 1975). More recently, the numerical formulation was somewhat changed to prevent nonphysical sources of angular momentum without affecting the conservation of enstrophy. This work will be reported in a further paper about atmospheric superrotation.

For the simulations presented below, two different horizontal resolutions were used: a low resolution with 24 latitudes from pole to pole and 32 longitudes, and

TABLE 1. Vertical discretization of the model: σ levels at the middle of the layers and corresponding heights in kilometers assuming a constant 10-km scale height of the atmosphere.

	Level														
	1	2	3	4	5	6	7	8	9	10	11	12	13	14	15
σ	0.996	0.987	0.966	0.923	0.847	0.735	0.596	0.447	0.309	0.197	0.116	0.062	0.030	0.011	0.022
z (km)	0.037	0.134	0.343	0.801	1.66	3.08	5.18	8.05	11.7	16.2	21.5	27.7	35.1	44.0	61.1

a high resolution with 48 latitudes and 64 longitudes. In both cases, points were regularly spread in both longitude and latitude (although the model, in its present version, allows one to zoom in on a given part of the globe). The vertical discretization is based on σ coordinates, where $\sigma = p/p_s$ is the pressure normalized by its local value at the surface. In the simulation the atmosphere was divided into 15 layers. The values of σ at the middle of the layers are given in Table 1 with corresponding approximate heights. The time integration is based on a leapfrog (explicit and center) scheme. The time step was fixed to 230 s for the high resolution and 500 s for the low resolution.

b. Radiation

The radiative transfer code is adapted from the one developed in the context of terrestrial modeling by Fouquart and Bonnel (1980) for solar radiation and Morcrette et al. (1986) for thermal radiation. This code, originally developed for the climate GCM of the Laboratoire de Météorologie Dynamique, has since been included by Morcrette in the operational model of the European Centre for Medium-Range Weather Forecasts (ECMWF).

1) THERMAL RADIATION

Effects of both atmospheric carbon dioxide and dust are included. Particular attention was given to the parameterization of absorption by the CO_2 15-μm band with inclusion of Doppler effect (Hourdin 1992). Cooling rates computations were carefully validated by comparison to line-by-line integrations. The model, in which Doppler effects are introduced, is very accurate up to 70 km. The thermal spectrum is divided into three parts: one for the core of the CO_2 15-μm band, one for the wings, and the third one for the remaining part of the spectrum. For the three parts, the transmission by dust is computed using a gray absorption approximation. For the two intervals of the CO_2 15-μm band, the total transmissivity is evaluated as the product between transmissivity of dust and that of carbon dioxide. Strictly speaking, it can be shown that this evaluation of the combined transmissivity is valid when there is no correlation between the spectral variations of the two absorbers. This is generally assumed for dust and carbon dioxide in the CO_2 15-μm band. Scattering is not taken into account because of the strong isotropy of the thermal radiation.

2) SOLAR RADIATION

In the original code developed by Fouquart and Bonnel (1980), the upward and downward fluxes are obtained from the reflectances and transmittances of the layers. The interaction between gaseous absorption and scattering (by dust, molecules, or clouds) is introduced using the photon path distribution method. At this stage, only absorption and scattering by dust (already present in the version of the code used at the ECMWF) are included in the Martian version although absorption by the near-infrared bands of carbon dioxide may become nonnegligible for very nondusty conditions. The transmittances and reflectances of the layers are computed using the Delta approximation to account for the strong asymmetry of the aerosol phase function.

3) ATMOSPHERIC DUST CONTENT

The atmospheric dust content is specified as a mixing ratio constant in both time and space, except for the vertical distribution, which is taken according to Pollack et al. (1990). Beyond simplicity, the reason for this choice is that dust transport has not been included in the GCM until now. This strong approximation may affect the global CO_2 condensation–sublimation cycle, which primarily depends on the local dust content at low latitudes (Pollack et al. 1990). The optical parameters of dust (such as single scattering albedo and asymmetry factor) are taken from Pollack et al. (1979).

c. Vertical turbulent mixing

The formulation of the vertical turbulent mixing is taken almost directly from the very simple scheme used in the LMD climate model. The effect of turbulent mixing on momentum and potential temperature is evaluated by the mean of a classical diffusion equation

$$\frac{\partial}{\partial t} = \frac{1}{\rho}\frac{\partial}{\partial z}\left(\rho K_z \frac{\partial}{\partial z}\right) \tag{1}$$

where the turbulent mixing coefficient K_z is computed as

$$K_z = le^{1/2} \tag{2}$$

in terms of mixing length l and a diagnostic estimate of the turbulent energy

$$e = \max\left\{ l^2\left[\left(\frac{\partial \mathbf{V}}{\partial z}\right)^2 - 2.5\,\frac{g}{\theta}\frac{\partial \theta}{\partial z}\right], e_{\min}\right\} \quad (3)$$

(the minimum value of the kinetic energy was set to $e_{\min} = 1 \times 10^{-6}$ m^2 s^{-1}). In the case where $e > e_{\min}$, the vertical mixing coefficient can be expressed as a function of the Richardson number

$$\mathrm{Ri} = \frac{g\partial\theta/\partial z}{\theta(\partial \mathbf{V}/\partial z)^2} \quad (4)$$

as

$$K = l^2\left\|\frac{\partial \mathbf{V}}{\partial z}\right\|\sqrt{1 - 2.5\,\mathrm{Ri}}. \quad (5)$$

For both momentum and potential temperature, the turbulent surface flux is computed as the product between the vertical gradient of the quantity (estimated between the surface value and that in the first atmospheric layer) and a drag coefficient C_D given by

$$C_D = C_{D0}[V_0 + \|\mathbf{V}_1\|] \quad (6)$$

where $\mathbf{V}_1$ is the wind in the first atmospheric layer and $V_0 = 1$ m s^{-1}. The diffusion equation is integrated with an implicit time scheme. In the simulations presented below, l was fixed to 35 m and C_{D0} to 2×10^{-3}, typical values used for terrestrial surfaces in the climate GCM.

d. Convective adjustment

Whereas much more sophisticated schemes for vertical turbulent diffusion may spontaneously simulate some kind of vertical convection (for example, see Mellor and Yamada 1974), our simple scheme (as many others) is not able to prevent subadiabatic vertical temperature gradients

$$\frac{\partial \theta}{\partial z} < 0. \quad (7)$$

If such an unstable profile is produced by the model, an adiabatic profile is immediately restored with a simple energy conserving scheme. If the resulting temperature profile is unstable at its upper or lower limit, this mechanism is instaneously extended in such a way that the final profile is entirely stable.

This convective adjustment is in fact achieved in a real atmosphere by parcel exchange through vertical convective motions. These motions not only transport energy but also momentum. The intensity of the momentum exchange is linked to the mass fluxes involved in the convection, which cannot be estimated in such a simple model. The best one can do is to compute an estimate of the instability of the atmosphere from the relative enthalpy exchange necessary to restore the adiabatic profile $\bar{\theta}$ from the original profile θ,

$$\alpha = \int |\theta - \bar{\theta}|\rho dz \Big/ \int \theta\rho dz. \quad (8)$$

When $\alpha < 1$ (this condition is always verified in the simulations), the angular momentum is entirely mixed on a fraction α of the mesh. This rather arbitrary choice is qualitatively acceptable in the sense that a larger instability will produce a larger momentum mixing.

e. Surface processes

Surface temperature evolution is governed by the balance between incoming fluxes (direct solar insolation, thermal radiation from the atmosphere and the surface itself, and turbulent heat fluxes) and thermal conduction in the soil. The parameterization of this last process is often rather crude in terrestrial GCMs, where a great part of the surface temperature is either imposed or computed in oceanic models. For a dry planet like Mars, an accurate parameterization of heat conduction is crucial to correctly determine surface temperatures and their response to diurnal, synoptic, and seasonal forcing. A new parameterization was therefore developed for the Martian version of the LMD GCM.

The time evolution of the temperature under the surface is given by a classical conduction equation

$$\frac{\partial T}{\partial t} = -\frac{1}{C}\frac{\partial F_c}{\partial z}, \quad (9)$$

where the conductive flux F_c is given by

$$F_c = -\lambda\frac{\partial T}{\partial z} \quad (10)$$

and where λ and C are the soil conductivity and specific heat per unit volume, respectively. In the simple case of a vertically homogeneous soil (which is assumed here), it can easily be shown that the model, as far as the time evolution of the surface temperature is concerned, is dependent only on the soil thermal inertia $I = \sqrt{\lambda C}$.

Although atmospheric GCMs often use force–restore schemes with one or two layers to simulate the time evolution of the surface temperature, it is much more accurate and straightforward to perform a direct temporal integration of these equations using a multilayer difference scheme in the ground (Jacobsen and Heise 1982; Warrilow et al. 1986). This was found to be numerically inexpensive enough even for a large number of layers in the soil: with 11 levels, this parameterization represents only 0.1% of the CPU time of the Martian GCM. The soil model is similar to that presented by Warrilow et al. (1981). The accuracy of the model was checked by computing the phase and intensity of the surface temperature oscillation forced by a sinusoidal varying surface flux. For periods in the range from 0.3 to 2000 sols, the model produces errors of less than 1% on the intensity and phase shifts lower than 0.02π.

f. Carbon dioxide condensation–sublimation

A condensation temperature is introduced, following Pollack et al. (1981), as

$$T_{CO_2} = 149.2 + 6.48 \ln p \qquad (11)$$

with T_{CO_2} in kelvin and pressure p in hectopascals. Both atmosphere and surface temperatures are prevented from falling below T_{CO_2} by precipitating atmospheric CO_2 onto the surface.

In the atmosphere: If the temperature of a given layer falls below T_{CO_2} (as an effect of dynamics or other physical processes), condensation occurs, in an amount appropriate to restore, by latent heat release, the condensation temperature corresponding to the local pressure. All condensed carbon dioxide instantly precipitates to the ground without sublimation. Surface pressure is modified in agreement with the total amount of precipitation.

At the surface: The temperature of the frost is kept at the condensation value either by condensing atmospheric CO_2 or by sublimating CO_2 ice.

The sublimation–condensation scheme exactly conserves both energy and mass. The energy balance on the caps is mainly controlled by albedo and emissivity of ice, which are unfortunately poorly known. The impact of those parameters on the annual pressure cycle has been carefully analyzed in a recent study by Pollack et al. (1993). Direct measurements (James et al. 1979; Paige and Ingersoll 1985) and model studies (Warren et al. 1990) yield large ranges of values: about 0.7–1.0 and 0.4–0.8 for emissivity and albedo, respectively. For this study, these quantities were somewhat arbitrarily fixed to 0.8 and 0.6, respectively (they were not tuned to fit Viking data).

g. Surface conditions

Three fields had finally to be specified at the surface: height of orography, thermal inertia, and albedo of ice free surface. Values obtained form the Viking measurements were used. These three fields, together with ice albedo and emissivity, and with the parameters defining the planet, its orbit, and its atmosphere, were the only prespecified parameters in the model.

3. Clear-sky simulations

a. Description

The first simulations presented here correspond to clear-sky conditions. Instead of using optical dust measured at the two Viking sites, we used optical depths deduced from the results of the Infrared Thermal Mapper (IRTM) experiment (Martin 1986) aboard Viking orbiters (Martin 1986), which offer a combined good spatial and temporal coverage (about one Martian year). The IRTM 9-μm atmospheric opacities exhibit a 0.51 mean value but a much lower mode value of 0.056 (Martin 1986). By comparison with Viking Lander measurements, these values are shown to be 2.5 times lower than visible dust opacities. The resulting mean dust opacity in the visible range is therefore 1.3 but the mode value, typical of clear-sky conditions, only 0.14. For the present clear-sky simulations the dust optical depth in the visible range (τ_{VIS}) was fixed to 0.2. From the study by Martin, the Viking sites appear as particularly dusty, which may be due, in a large part, to their location well below the mean Martian height. Of course, the very simple specification of the atmospheric dust content cannot represent all the complexity of the real situation, such as the systematic increase in dust optical depth during northern winter, even for years without global dust storm.

Full orography was included. Solar heating was computed using a diurnally averaged incoming solar flux since the diurnal cycle had been found, in some test experiments, not to significantly affect the seasonal pressure cycle. This allows us to save computational time. It must be noticed, however, that we have since then performed more than 50 years of simulations with a complete calculation of insolation 20 times per day.

One parameter remained to be determined: the total mass M of CO_2 including atmosphere and caps. This mass can be represented by an equivalent total surface pressure p_{tot} with $p_{tot} = gM/(4\pi a^2)$ (a and g are, respectively, the planetary radius and gravity). When no polar caps are present, p_{tot} is just the mean surface pressure p_{atm}. With polar caps, the equivalent total pressure can be separated as $p_{tot} = p_{atm} + p_{caps}$ where p_{caps} is an equivalent pressure for this part of the carbon dioxide trapped in the caps.

In order to fix the value of p_{tot}, a first numerical simulation was performed over two Martian years with the low horizontal resolution (24 latitudes and 32 longitudes), starting from a state with no wind, no polar caps, and an isothermal atmosphere at 200 K, for an arbitrary value of $p_{tot} = p_{atm} = 8$ hPa.

The polar caps spontaneously formed in this simulation and the system was found to equilibrate in less than one year. The pressure fluctuations at the Viking landing sites were compared to observations. The total atmospheric mass was then shifted in order to change the mean pressure at those two points to their observed values. The equivalent total atmospheric pressure was thus set to $p_{tot} = 7.2$ hPa.

A new simulation was then performed, starting once again from an isothermal state of rest with no polar caps. The evolution of the surface pressure at both Viking landing sites is reported in Fig. 2. During the first summer, the pressure rapidly decreases due to the formation of the south polar cap but the northern cap has not yet formed. From the middle of the first year, after the sublimation of the south cap, the initial conditions seem to be essentially forgotten and the pressure

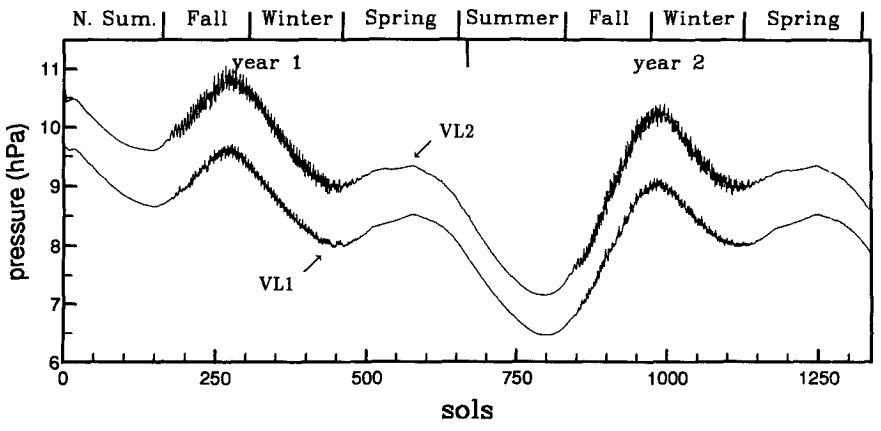

FIG. 2. Evolution of the simulated pressure at both Viking landing sites during the first two years of the low-resolution simulation.

oscillation to be very well reproduced from one year to the other.

The simulation was then carried further with the high horizontal resolution (48 latitudes and 64 longitudes) over one Martian year starting from the final state of the low-resolution simulation ($L_s = 97°$). The high-resolution simulation (Fig. 3) will be referred to as the "reference simulation" in what follows.

b. *Model validation*

The purpose of this paper is not to give a complete validation of the GCM (this will be addressed in a forthcoming publication) but to underline the influence of dynamics on the spatial distribution of the atmospheric mass. Nevertheless, since this is the first publication showing results of the LMD Martian GCM, we will present some comparisons to observations and to other numerical simulations.

Tracers of the atmospheric circulation are rather uncommon on Mars. Except during dust storms, cloud features (either dust, CO_2, or H_2O clouds) are restricted to particular seasons and locations. The only information giving a global spatial coverage is the retrieval of temperature from the observation of the emitted thermal radiation. Only *Mariner-9* had enough spectral and spatial coverage to allow determination of complete maps (at least in a latitude–altitude frame) of the atmospheric thermal structure. The IRTM instrument, aboard Viking, had only one wide 15-μm channel sensitive to atmospheric temperatures and did not give any information on the vertical thermal structure. Figure 4 shows a comparison between the temperature field deduced from *Mariner-9* measurements during spring (upper panel), L_s = 43 to 54, and the field of the reference simulation (middle panel). The model reproduces the main characteristics of the observed thermal structure such as the very weak latitudinal temperature gradients between 20°S and 60°N with a mean temperature of about 215 K near the surface.

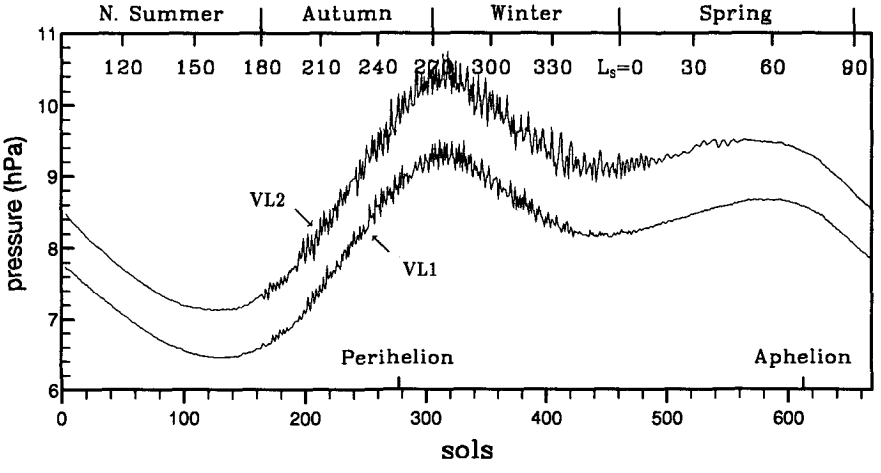

FIG. 3. Evolution of the surface pressure at the two landing sites in the reference simulation.

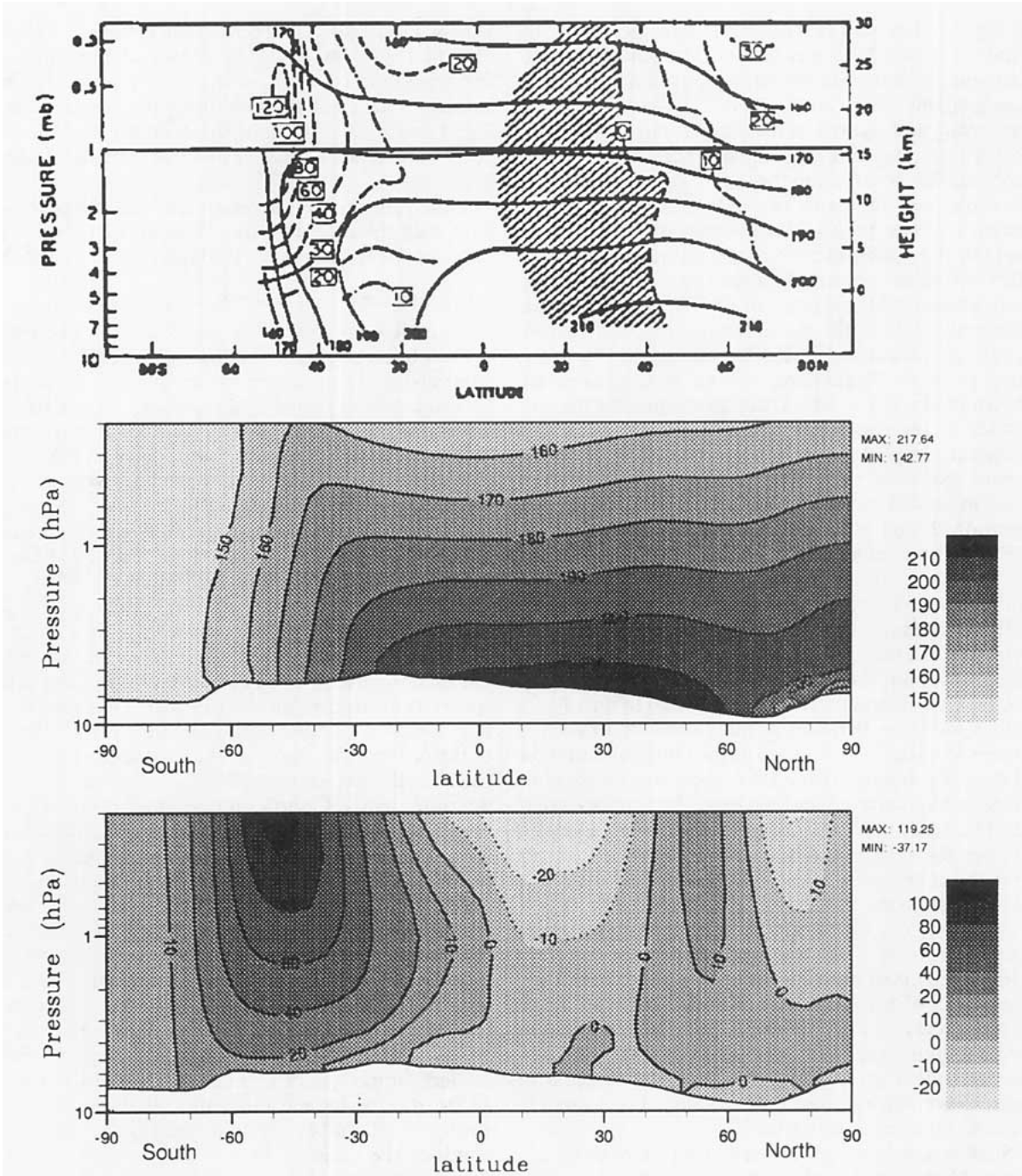

FIG. 4. Comparison of the results of the reference simulation to *Mariner-9* data during northern spring (L_s = 43°–54°). The solid curves of the upper panel show the temperatures (in *K*) as retrieved from the results of the IRIS experiment. The dashed–dotted curves show the zonal wind (in m s^{-1}) as deduced from the thermal wind balance (Pollack et al. 1981). The middle panel shows the simulated temperature (in *K*) for the same season and the lower panel the simulated zonal wind (in m s^{-1}).

The latitudinal temperature gradient, at the edge of the forming cap, near 50°N is also very well simulated even if there are some discrepancies in the vertical structure in this particular region. Finally, at least in the northern midlatitudes, the vertical temperature gradient is very well simulated, the temperature falling from 215 K near the surface to 160 K at the 0.3-hPa level. Based on the thermal wind equation (generally assumed to be accurately valid on Mars), it is possible to retrieve winds from the temperature field, which has been done for the *Mariner-9* measurements (superimposed on the temperature field in the upper panel

of Fig. 4). This can be compared with the simulated winds in the GCM (lower panel). The main feature is a unique jet, linked to the strong latitudinal temperature gradient of the southern hemisphere. The jet is less strong and narrow in the simulation.

If remote sounding gives the best spatial coverage of any available observation for the Martian atmosphere, the direct measurements of winds, pressure, and temperature at two points of the surface over successive years by the Viking missions are a unique fact in planetary sciences. Pressure data are the most interesting from a meteorological point of view since they contain information about the global atmospheric circulation, as already mentioned in the Introduction. The simulated pressure fluctuations at both landing sites are shown in Fig. 3. The simulation overestimates the amplitude of the seasonal variation by about 20% with some shift in phase, but the agreement is in fact quite remarkable if one remembers that no parameter except total mass was tuned in the simulation. As already mentioned and studied in detail by Pollack et al. (1993), the annual pressure cycle is very dependent on the values chosen for the dust opacity and the ice emissivity and albedo. Reduction of either albedo or emissivity results in a smaller mass of the caps and therefore in a less pronounced seasonal pressure cycle. The values of those parameters are unfortunately poorly known, and moreover, the tuning to unrealistic values for those parameters may allow us to correct some model deficiencies such as the nonrepresentation of the polar hoods arising from the atmospheric condensation of carbon dioxide above the forming polar cap (Pollack et al. 1993). As shown by Pollack et al. (1993), the variations of the atmospheric dust content over the course of the year also significantly affect the seasonal pressure variations. However, the tests performed with our GCM, in the range of clear-sky opacities $\tau_{vis} < 1$, were not able to correct the discrepancy with the observed pressure variations. On the contrary, the tuning of the ice albedo and emissivity seems to be able to give a much better agreement, as suggested by new numerical experiments run at LMD (in fact, the equivalent pressure p_{tot} must also be adjusted in order to keep the mean surface pressure, at both landing sites, to their observed values).

Such a tuning is very important to establish an accurate Martian climatology, or for engineering applications, and will be reported in a forthcoming paper. For the present work, it was not so crucial since we are only interested by the spatial variations of the difference between the local pressure and its planetary mean p_{atm}. This difference essentially depends on the thermal and dynamical atmospheric structure and not on the absolute value of p_{atm}.

Another element of validation is the comparison between simulated and observed statistical properties of the transient eddies. This has not been addressed yet in detail but there is a global agreement in period (between 2 and 5 sols) and amplitude (about 0.5 hPa for *VL1* and 0.25 for *VL2*). Moreover, the evolution of the amplitude on the course of the year is very well simulated, as clearly visible from the comparison of Fig. 1 and Fig. 3 (the comparison must be done with years 2 and 3 of the mission where no global dust storm occurred).

Finally, the numerical results are in global agreement with that obtained with the Ames GCM for clear-sky conditions (Pollack et al. 1981; Pollack et al. 1990).

c. *Atmospheric circulation near solstice*

Since it is important for the following discussion, we will briefly describe the main characteristics of the Martian global atmospheric circulation, particularly focusing on the period near northern winter solstice. The simulated temperature, meridional circulation, and zonal wind at $L_S = 287°$ are shown in Fig. 7. The temperature and zonal winds have been averaged over longitudes (zonal mean) and time (over five consecutive days). Those results are in very good agreement with those obtained by Haberle et al. (1993) for the same period with a dust optical depth $\tau_{vis} = 0.3$.

The situation is rather different from what is observed on Earth at the same season. Near solstice for both planets (which have almost the same obliquity), the incoming solar radiation at the top of the atmosphere is maximum on the summer polar region. On Earth, indeed, because of the very high thermal inertia of the oceans, the maximum surface temperature (the so-called thermal equator) does not oscillate in latitude by more than 15° north and 5° south of the equator. On the contrary, on Mars the surface thermal inertia is very weak; at $L_S = 287°$, the temperature is maximum in southern high latitudes and rather uniform over the southern hemisphere, in contrast with a strong latitudinal temperature gradient at the edge of the polar cap. This gradient is associated through geostrophic balance with a strong eastward zonal jet (between 30° and 70°N). This is also the location of the strong baroclinic activity responsible for the short period fluctuations of the surface pressure observed by the Viking landers (upper panel of Fig. 1). Between 40°S and 40°N, the meridional circulation is dominated by a strong direct Hadley cell, with maximum meridional winds of the order of 10 m s^{-1}. The zonal winds in this region are analogous to the terrestrial trade winds (mainly constrained by the combination of meridional advection of angular momentum and surface friction) except that, because of the deeper extension of the Hadley cell into the summer hemisphere, strong eastward winds are produced in low southern latitudes. The strong near-surface positive wind, centered at 25°S, is in fact analogous to the winds of the terrestrial Indian monsoon. In that case on Earth, because of the presence of the Asian continent, the Hadley circulation crosses the equator much farther than in the planetary mean, resulting in a strong eastward current over India.

4. The annual pressure cycle

Comparison of the simulated pressure at different locations showed the rather unsuspected fact that the time evolution of the surface pressure, in rather good agreement with Viking data for the two landing sites, varies a lot with latitude. This is illustrated in the upper panel of Fig. 5, representing the time evolution of the zonally averaged surface pressure for four different latitudes, 75°N, 37.5°N, 37.5°S, and 75°S, as well as the average pressure p_{atm}, which is proportional to the total atmospheric mass. Only this last curve is a direct signature of the condensation–sublimation cycle of carbon dioxide.

The differences in the pressure annual means at these various latitudes are due to the differences of the mean heights. But even with subtraction of the mean annual value from these different curves, large differences between latitudes still remain.

For example, the relative difference between pressures at 37.5°N and 37.5°S evolves from 15% near northern summer solstice to 24% at northern winter solstice. This time variability is even much more marked for polar latitudes. As a consequence, the mean pressure cycle is much more symmetric than the Viking measurements; in *VL1* data, for example, the northern spring pressure maximum is 7% below the northern winter solstice maximum (6.7% for the simulation) but the relative difference is only 2.4% in the planetary mean of the simulated pressure. Moreover, the northern spring maximum in the 37.5°S signal is higher than the winter solstice maximum.

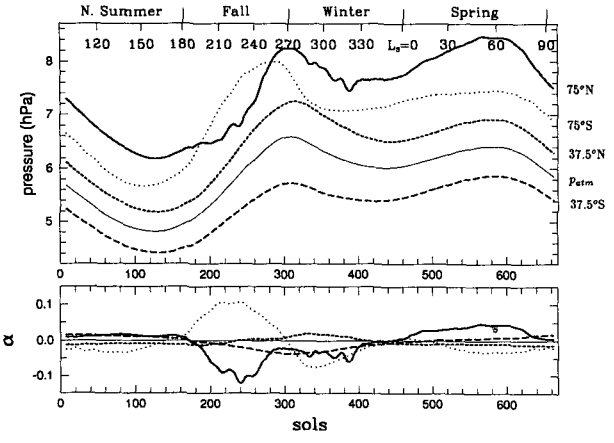

FIG. 5. Annual pressure fluctuation for various latitudes (reference simulation). The pressures were averaged along a given parallel and over ten consecutive days, which allows smoothing the main part of the high-frequency synoptic oscillations. Conventions for the various curves: mean pressure at 37.5°N (short dashed), 37.5°S (long dashed), 75°N (solid), and 75°S (dotted). The upper panel shows the simulated pressure p_s, and the thin solid curve is the planetary mean of the pressure p_{atm} proportional to the total atmospheric mass. The lower panel shows the meteorological contribution as defined by $\alpha = p/p_{atm} - \langle p/p_{atm}\rangle_t$ where $\langle\rangle_t$ is the annual mean (see text).

In order to eliminate the condensation–sublimation cycle, the longitudinally averaged surface pressure was divided by the globally averaged surface pressure p_{atm}. The annual mean $\langle p/p_{atm}\rangle_t$ was then subtracted in order to retain only the relative temporal variations. This can be interpreted as the meteorological contribution to the atmospheric pressure cycle (but does not include the systematic latitudinal effects). The time evolution of $\alpha = (p/p_{atm}) - \langle p/p_{atm}\rangle_t$ is reported in the lower panel of Fig. 5 for the same four latitudes. This is analogous to the differential weather introduced by Pollack et al. (1993). This meteorological contribution accounts for a 5% temporal variation in midlatitudes and for 15% to 20% in high latitudes. At 75°N, it is comparable to the amplitude of the total pressure oscillation, which is of the order of 25%.

a. *Orographic effect*

Hess et al. (1979) already discussed the possible effect of the temperature variations on the Viking pressure oscillations. In addition to differences in mean pressure values, latitudinal variations of altitude modulate the pressure cycle through temperature variations. At northern winter solstice, the temperature is low in the northern hemisphere ($T \sim 180$ K), inducing a small vertical atmospheric scale height ($H \sim 9.2$ km). A great part of the atmosphere is then trapped in the low-altitude northern regions, thus decreasing the pressure of the southern hemisphere, which is 2 km higher on the average. The opposite happens during the northern summer when part of the air is ejected from the low northern regions ($H \sim 11.8$ km for $T \sim 230$ K). Quantitatively, this leads to a northern pressure 21% higher than the southern pressure at northern winter solstice but only 17% higher at summer solstice. This is consistent with the simulated pressures at 37°N and 37°S. But this hydrostatic analysis is based on the hypothesis that the pressure is constant with latitude for a given equipotential height, which is far from verified in reality.

b. *Dynamical effect*

It is well known that for all known rapidly rotating planets, the horizontal pressure gradients and winds are coupled by the classical geostrophic balance. The latitudinal pressure variation and zonal wind are related by

$$2\Omega \sin\phi u \sim -\frac{RT}{p}\frac{\partial p}{a\partial\phi} \qquad (12)$$

(ϕ is latitude, R the gas constant, a the radius of the planet, and Ω its rotation rate); for an atmospheric parcel rotating faster than the solid planet ($u > 0$), the inertial Coriolis force $2\Omega \sin\phi u$ is equatorward and is thus balanced by a decrease of pressure toward the pole. This balance is only valid above the planetary boundary

layer (PBL), typically 1 km high on Earth. Within the PBL, the wind amplitude decreases to become zero at the surface with an associated change in its direction classically approximated by the so-called Ekman spiral (the basis of the theory of the planetary boundary layer can be found, for example, in Holton 1979, p. 101–118). But even for surface fields, this balance still remains qualitatively correct as illustrated on Earth, in the "roaring forties" during winter, by the balance between the equatorward pressure gradient and the eastward surface winds between 30°S and 60°S (Fig. 8).

1) Dynamical effect: simulation without mountains

This effect is particularly easy to identify in the roaring forties on Earth because of the absence of continents. But on Mars, as already mentioned, the surface pressure field is primarily dominated by orography. In order to isolate the dynamical effect, the low-resolution version of the GCM was integrated without mountains over two Martian years in exactly the same conditions as for the reference simulation. Figure 6 shows the time evolution of the meteorological contribution $(p/p_{\text{atm}}) - \langle p/p_{\text{atm}} \rangle_t$ for the same four latitudes as for Fig. 5. Those curves really represent the effect of dynamics on the annual pressure cycle. Comparison with the lower panel of Fig. 5 clearly shows that the dynamical effect can explain part of the spatial variability of the seasonal pressure fluctuations, especially for high latitudes. For example, the maximum and minimum of the four curves occur at the same season for the two simulations. For high latitudes, the dynamical effect may represent the main contribution to the local component of the pressure variation. This effect seems to be relatively weaker for lower latitudes.

The longitudinally averaged surface pressure (dashed curve) and zonal wind (solid curve) near northern winter solstice $L_s = 288°$ are shown in Fig. 9. The geostrophic relationship between the zonal wind and surface pressure appears very clearly: the equatorward Coriolis force associated with the lower part of the winter jet (between 40°N and 90°N) is balanced by an equatorward pressure gradient. The same is observed for the near-surface positive jet (analogous to the terrestrial monsoon winds) between 25° and 35°S. In fact, this relationship is even numerically correct: the zonal

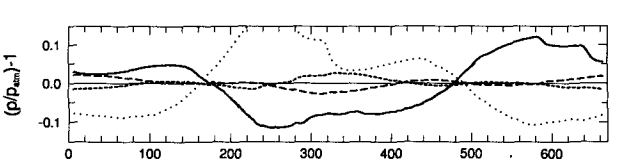

FIG. 6. Annual pressure cycle as simulated without mountains. (see text for complementary information). Time evolution of $(p/p_{\text{atm}}) - \langle p/p_{\text{atm}} \rangle_t$ for various latitudes. Same conventions as for Fig. 5.

wind simulated at 300 m above the surface (full line of Fig. 9) is very close to the wind deduced from Eq. (12) using the surface pressure and the temperature simulated in the first atmospheric layer. The geostrophic solution is not computed for latitudes lower than 10° because of the singularity of Eq. (12) in that region.

The agreement with the geostrophic wind, computed from the surface pressure gradient, is not as good for winds simulated at other heights. Below 300 m, the wind is strongly reduced by vertical diffusion and does not balance the latitudinal pressure gradient; above the third layer, the geostrophic balance is better satisfied but the latitudinal pressure variations become significantly different from their surface values, being affected by the latitudinal variations of the atmospheric scale height. This is in good agreement with what is known from the well-studied terrestrial PBL: the vertical wind gradient is generally sharp in the first few hundred meters above the surface but, above 300 to 400 m, both amplitude and direction are within 10% or 20% of their asymptotic values at the top of the PBL, generally located at about 1 km (see Holton 1979, p. 111).

2) Separation between dynamical and orographic effect

In the presence of mountains, the distinction between orographic and dynamical effects can be made rather directly by an alternate version of the geostrophic equation [Eq. (12)] derived using the normalized pressure $\sigma = p/p_s$ (as in the GCM formulation) instead of height as a vertical coordinate. The geostrophic relationship then becomes

$$2\Omega \sin\phi u \sim -\frac{RT}{ap_s}\frac{\partial p_s}{\partial \phi} - \frac{1}{a}\frac{\partial \Phi}{\partial \phi} \qquad (13)$$

in which the latitudinal variation of the surface pressure is given as the sum of a contribution linked to the presence of zonal winds (left-hand side) and another contribution due to the latitudinal variations of height (last term on the right-hand side).

As for the simulation without mountains, the zonal wind simulated in the third layer of the model (full curve in Fig. 10) is very close to that deduced from the geostrophic Eq. (13) (dotted curve) using the surface pressure, the surface geopotential, and the air temperature near the ground.

Based on this numerical agreement, Eq. (13) can be used to decompose the surface pressure as the sum of three terms,

$$p_s = p_{\text{atm}} + p_{\text{dyn}} + p_{\text{oro}}, \qquad (14)$$

whose temporal variations represent the respective effect of condensation–sublimation, dynamics, and orography. The first term p_{atm} is, as before, the globally averaged surface pressure. The dynamical contribution p_{dyn} is defined by

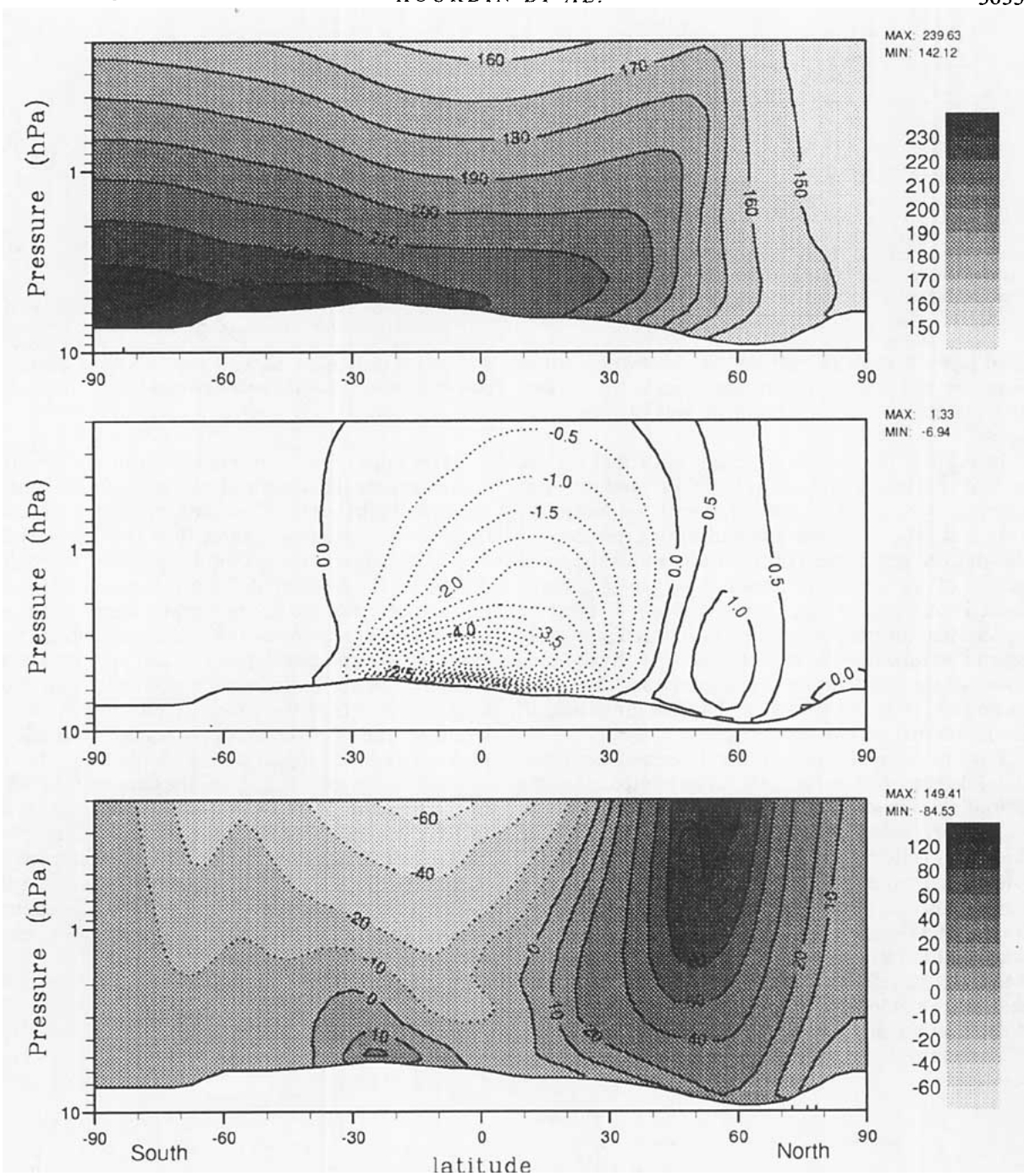

FIG. 7. Zonally averaged atmospheric structure at $L_S = 287°$ (reference simulation). Upper panel: temperature in K. Middle panel: streamfunction of the meridional circulation in 10^9 kg s^{-1}. The ascending branch of the Hadley circulation is that located between 20° and 30°S. The meridional wind is southward near the surface between 40°N and 40°S. Lower panel: zonal wind (in m s^{-1}).

$$\frac{1}{a}\frac{\partial p_{\text{dyn}}}{\partial \phi} = -\frac{2 p_s \Omega \sin\phi u}{RT} \qquad (15)$$

with the condition that the planetary mean of p_{dyn} must be zero. Similarly, the orographic contribution p_{oro} is defined by

$$\frac{1}{a}\frac{\partial p_{\text{oro}}}{\partial \phi} = -\frac{p_s}{aRT}\frac{\partial \Phi_s}{\partial \phi} \qquad (16)$$

with a planetary mean equal to zero. In Eqs. (15) and (16), Φ_s is the surface geopotential, T the temperature in the first GCM layer, and u the zonal wind in the

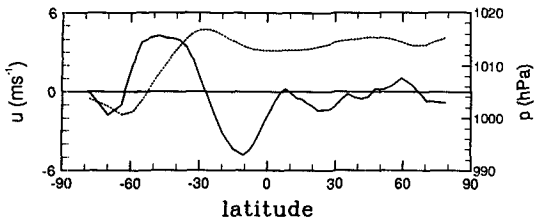

FIG. 8. Zonally averaged zonal wind u and surface pressure p for mean July conditions on Earth. The zonal wind (solid) is that simulated at the first level of the LMD climate GCM (at about 90 m above the surface). The dashed curve is the simulated surface pressure.

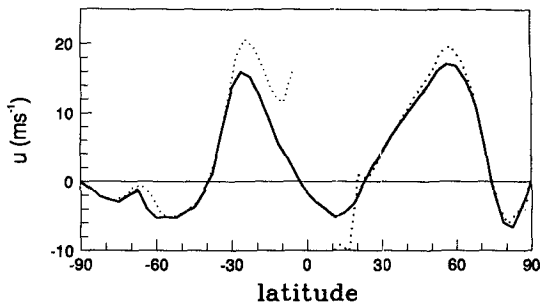

FIG. 10. Zonal wind near northern winter solstice ($L_s = 288°$) for the reference simulation. The solid curve shows the zonal wind simulated in the third layer of the GCM (at about 300 m above the surface) and the dotted curve represents the wind as deduced by geostrophic balance with the surface pressure [Eq. (13)].

third layer. It must be noticed that the two contributions are not strictly independent since the surface pressure appears on the right-hand side of both equations.

In Fig. 11, the zonally averaged simulated surface pressure p_s (thin solid line) at $L_s = 288°$ and the pressure $p_{atm} + p_{dyn} + p_{oro}$ (dotted), computed from Eqs. (15) and (16) and then longitudinally averaged, are shown to be very close. The figure also shows the zonal means of the two contributions: $p_{atm} + p_{oro}$ (long dashed) and $p_{atm} + p_{dyn}$ (short dashed). It must be noticed that the orographic effect introduced previously is just that linked to the modulation of p_{oro} by the variations of the temperature over the course of the year; its amplitude is much weaker than the amplitude of the latitudinal variations of p_{oro}.

For this particular season, the dynamical contribution (short dashed in Fig. 11) can be compared to the latitudinal variations of pressure simulated without mountains (dashed in Fig. 9). The differences are, of course, directly related to the differences in the simulated zonal winds (Fig. 9 for the simulation without mountains and Fig. 10 for the reference simulation). If the general pattern is similar, it can be noticed, indeed, that the analogs of the terrestrial trade winds are weaker in the reference simulation and that the winter eastward jet is located at a slightly lower latitude (the differences are due not only to the absence or presence of mountains but also to the differences in horizontal resolution).

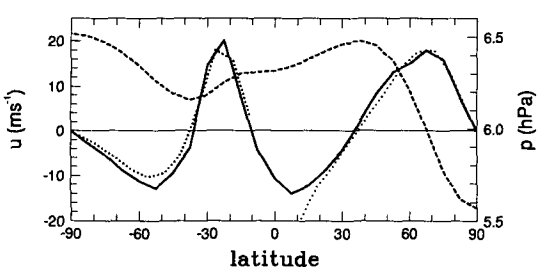

FIG. 9. Longitudinally averaged surface pressure (dashed curve, scale on the right) and zonal wind (solid curve, scale on the left) near northern winter solstice ($L_s = 288$) in a simulation without mountains. The zonal wind is taken at the third model level (about 300 m above the surface). The dotted curve shows the geostrophic wind deduced from surface pressure by Eq. (12).

At the edge of the northern polar cap, the structure is analogous to that described previously for the roaring forties on Earth but the effect is much stronger on Mars: the pressure decreases by more than 16% between 30° and 70°N, whereas the maximum variation is less than 2% on Earth. Another difference between Mars and Earth arises from the strong thermal inertia of the terrestrial oceans. Because of this, the atmospheric thermal structure and meridional circulation remain much more symmetric (with respect to equator) on Earth than on Mars over the course of the year. As a consequence, the jet of the terrestrial southern middle latitudes does not disappear during southern summer (its intensity is just reduced). Thus, the temporal variations of the pressure, as measured at a fixed point on the surface, are much weaker than the maximum 2% of the latitudinal pressure variation. On the contrary, the jet totally disappears during summer on Mars (as visible in Fig. 10 and lower panel of Fig. 7). Consequently, the amplitudes of the temporal and spatial pressure variations are rather similar.

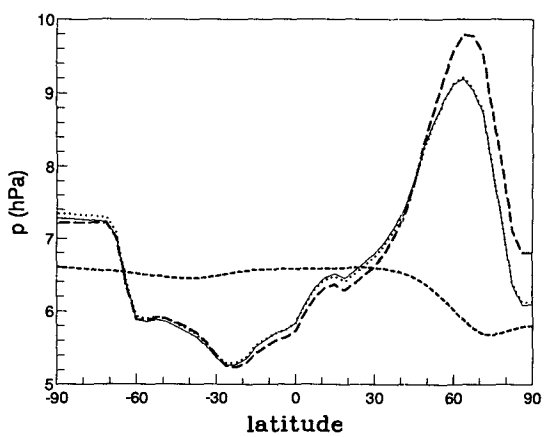

FIG. 11. Surface pressure near northern winter solstice ($L_s = 288°$) for the reference simulation. The simulated surface pressure (thin solid curve) is compared to $p_{atm} + p_{oro} + p_{dyn}$ (dotted curve) of the dynamical $p_{atm} + p_{dyn}$ (small dashed) and orographic $p_{atm} + p_{oro}$ (long dashed) contributions as introduced in the main text.

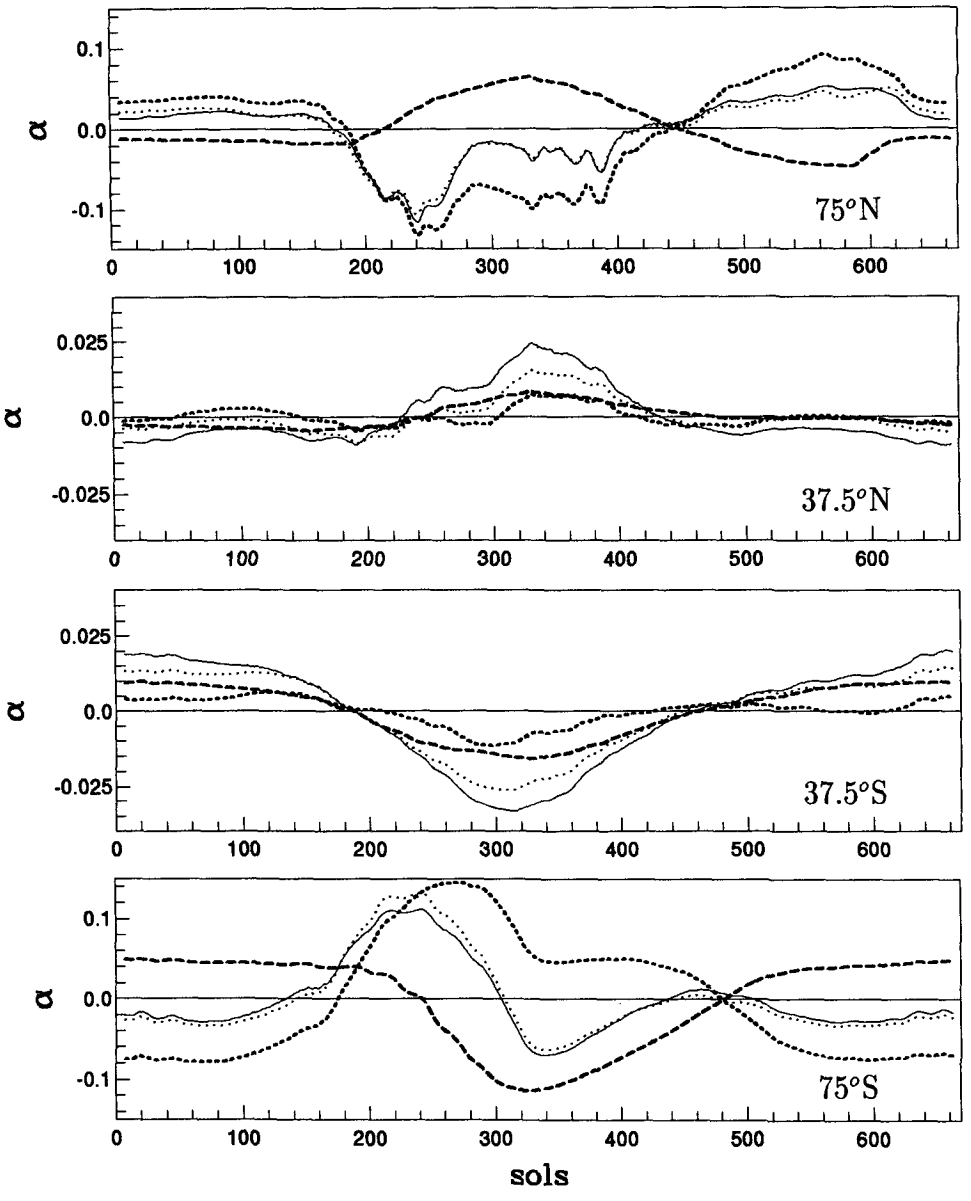

FIG. 12. Time evolution of the dynamical and orographic contributions to the mean surface pressure at four different latitudes (reference simulation). For each latitude, the sum (dotted) of the dynamical α_{dyn} (short dashed) and orographic α_{oro} (long dashed) contribution is compared to the simulated evolution of $\alpha = p/p_{atm} - \langle p/p_{atm} \rangle_t$ (thin solid curve) with $\alpha_{dyn} = p_{dyn}/p_{atm} - \langle p_{dyn}/p_{atm} \rangle_t$ and $\alpha_{oro} = p_{oro}/p_{atm} - \langle p_{oro}/p_{atm} \rangle_t$.

The differential effect between the latitude of *VL1* and *VL2* is very different from that simulated without mountains. The effect is much stronger and the pressure is lower by 24% at 48°N than at 22°N. The effect may partly counteract the orographic effect, particularly strong for both landing sites since *VL2*, the most poleward of the two landers, was located about 1 km below *VL1*.

Finally, the separation between orographic and dynamical components can be used to analyze the time evolution of the meteorologic contribution α introduced previously. Each panel in Fig. 12 corresponds to one of the latitudes analyzed in Fig. 5 and shows the decomposition of the total meteorological contribution α, in terms of $\alpha_{dyn} = (p_{dyn}/p_{atm}) - \langle p_{dyn}/p_{atm} \rangle_t$ and $\alpha_{oro} = (p_{oro}/p_{atm}) - \langle p_{oro}/p_{atm} \rangle_t$. For all latitudes, the largest difference between the simulated α and the sum $\alpha_{dyn} + \alpha_{oro}$ is of the order of 0.01.

In midlatitudes (37.5°): 1) The dynamical contribution is generally weaker than the effect of orography; 2) both α_{dyn} and α_{oro} are rather weak (the amplitude of the seasonal variation is of the order of 0.02); but

3) they tend to reinforce each other, leading to an amplitude of 4%–5% for the total meteorological contribution.

For high latitudes (75°): 1) The dynamical effect is generally stronger than the orographic contribution; 2) both contributions are much stronger than in lower latitudes (of the order of 0.2); but 3) they generally counteract each other. At 75°S, the amplitude of the temporal variation of α_{dyn} is about 0.25, which means that the dynamical effect is responsible for a variation of the surface pressure of about 25% over the course of the year. This variation has the same magnitude as that linked to the condensation–sublimation cycle.

c. *Dynamical effect during dust storms*

In effect, the variation of pressure at both Viking landing sites during the 1977-B great dust storm is a direct evidence for the dynamical effect: at the beginning of the storm, the pressure (smoothed from synoptic oscillations) jumped by about 0.5 hPa at *Viking Lander 2* whereas the maximum effect at *Viking Lander 1* was only 0.2 hPa. This has already been noticed and studied in detail by Pollack et al. (1993).

This period was investigated performing a new simulation with the high-resolution LMD GCM, starting from the atmospheric state at $L_S = 274°$ produced by the reference simulation. Only the total dust optical depth was changed from 0.2 to 2.5 ("dust storm simulation"). Once more, this is a strong simplification

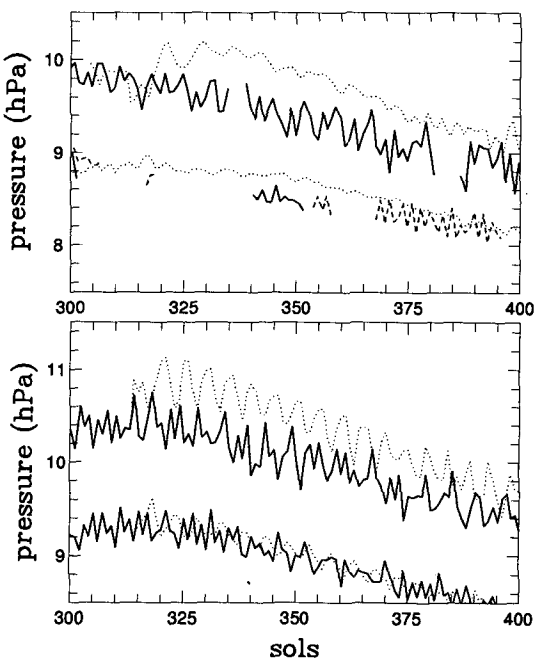

FIG. 13. Pressure at both Viking landing sites as measured by the probes (upper panel) and simulated by the LMD GCM (lower panel). Upper panel: the Viking pressure data are plotted with the same conventions as for Fig. 1: year 1 (dotted), 2 (solid), and 3 (dashed). Lower panel: numerical results of the two high-resolution simulations: the reference simulation (solid) corresponding to $\tau_{VIS} = 0.2$; the dust storm simulation (dotted) with $\tau_{VIS} = 2.5$.

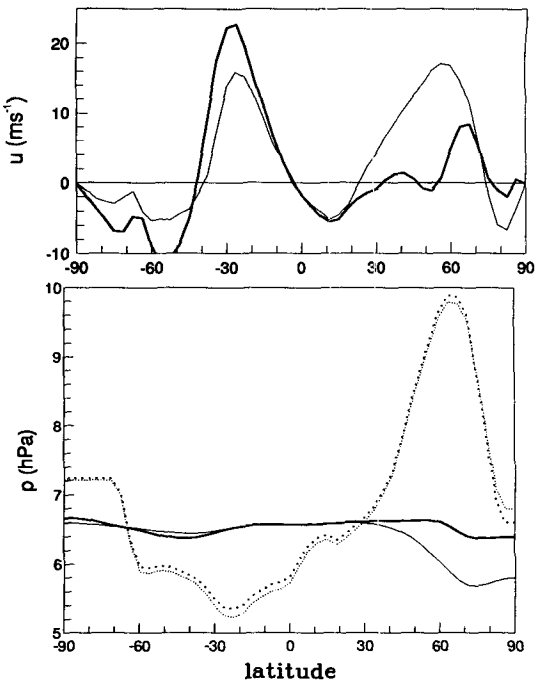

FIG. 14. Change in zonal wind and surface pressure during dust storm (at $L_s = 288°$). In both panels, the thin curves refer to the reference simulation and the heavy curves to the "dust storm" simulation. The upper panel shows the zonal wind (m s^{-1}). The lower panel shows the comparison of the dynamic (solid) and orographic (dotted) contributions to the surface pressure.

of the real situation in which the mean optical depth, generally already high near northern winter solstice, jumped suddenly to extremely high values (reaching a value of 5 at the *VL1* landing site) and then decreased slowly. However, even the use of time variation of the mean optical depth would be far from realistic since the dust content and its evolution were highly variable in space.

A direct confirmation of the dynamical effect on the pressure cycle can be seen in Fig. 13. The upper panel shows the Viking pressure observations between sols 300 and 400; the lower panel shows the simulated variations of pressure at the two Viking sites in the reference simulation and in the "dust storm" simulation. In the latter, baroclinic activity is not reduced as much, in comparison with the reference, as in observations. The change in periodicity, on the other hand, is better simulated. More important for our particular purpose, the behavior of the mean pressure (smoothed from baroclinic fluctuations) is in very good agreement with the observations: by comparison with clear-sky situations, the pressure is increased by about 0.5 hPa at *VL2* but only 0.1 hPa at *VL1*. This change in the mean pressure is directly related to the modification of the global atmospheric circulation: both the intensity and the latitudinal extent of the Hadley cell are strongly increased, as also found in other numerical simulations (Haberle et al. 1982); the monsoonlike jet is reinforced and the eastward winter jet is reduced and shifted to higher latitudes. This is illustrated in the upper panel of Fig.

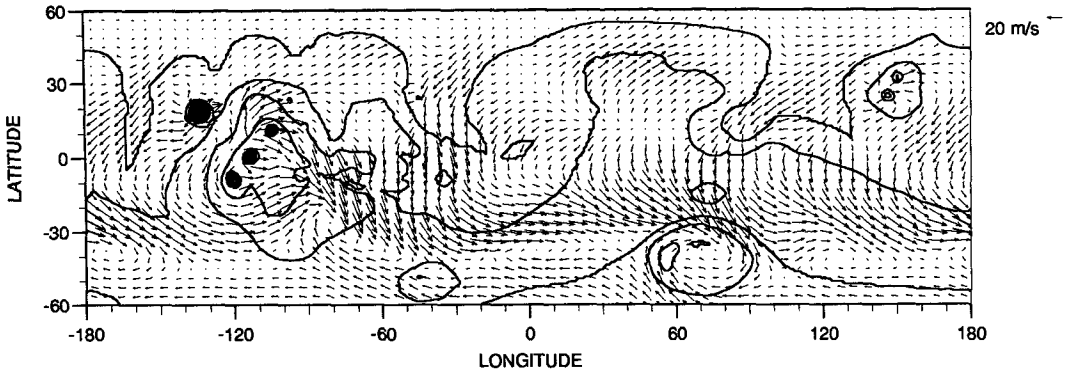

FIG. 15. Wind map from the dust storm simulation, 300 m above the surface, at L_s = 300°. The line contours correspond to the Martian orography and are spaced each 3 km.

14. The orographic contribution to the surface pressure was almost unchanged in the northern midlatitudes but the dynamical contribution was strongly increased in high latitudes. The dynamical effect contributes to an increase of about 0.25 hPa of the mean pressure at 48°N whereas the pressure at 22°N is not affected. Thus, the differential effect in the evolution of surface pressures at both Viking sites clearly appears as a consequence of this dynamical effect.

This simulation is particularly interesting since it gives a unique opportunity for new model validations. Bright streaks [Type I(b), e.g., see Magalhaes 1987], observed all over the planet, are generally believed to form in the waning phase of global dust storms, by dust deposit in the lee of impact craters. Therefore, the observation of those streaks allows one to construct a global map of the wind directions for this particular period (Magalhaes 1987; Zurek et al. 1992). The near-surface winds from the dust storm simulation at L_s = 300° are shown in Fig. 15. The directions are in very good agreement with those deduced from the observations of Type I(b) streaks. The analogy to the Indian monsoon is very clear on this map. The highly axisymmetric strong eastward jet is centered at 30°S, exactly as in the wind data. The structure of the flow, clearly influenced by orography, is also very well simulated.

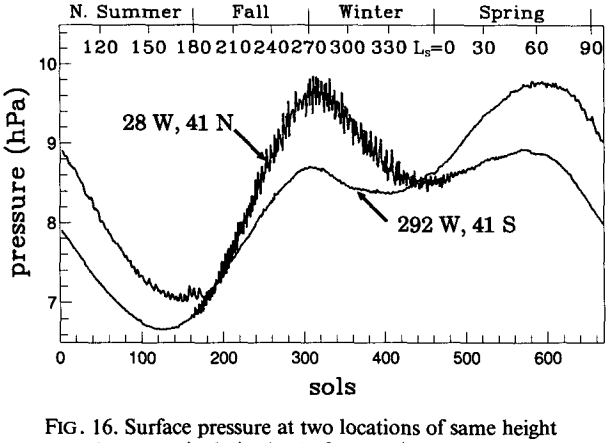

FIG. 16. Surface pressure at two locations of same height but opposite latitudes (reference simulation).

Another very interesting observational constraint for this particular season is the change in the wind direction at *VL2* at the beginning of the dust storm: the wind, predominantly westerly before the dust storm, turned to northeasterly during the storm. This change is very well simulated by the LMD GCM.

d. Local effects

At this point, we have only considered zonally averaged fields and latitudinal effects. Locally, the variations can be much larger, as illustrated by Fig. 16, which shows the pressure cycle at two points at about the same height but opposite latitudes. The first one is located at 41°N, at about the same height and latitude as *VL2*, and the second at 41°S, at the bottom of Hellas Planitia, a low plain situated 5 km below the 41°S mean height. At this location, the orographic effect is strongly reinforced: at southern winter solstice, for example, when the enhancement of the pressure by the orographic effect is maximum in the Southern Hemisphere, the ratio of the pressure at the bottom of Hellas Planitia to the mean pressure at the same latitude is also maximum because of the local small atmospheric scale height (not shown). What would have been the condensation–sublimation rates of the polar caps deduced from a unique Viking lander located in Hellas Planitia? This also illustrates the high difficulty of deriving the pressure surface field, which is coupled with both orography through hydrostatic balance and winds through geostrophic balance, a question that can hardly be addressed without a global numerical model.

5. Concluding remarks

The Viking mission has shown that the Martian surface pressure varies by about 25% over the course of the year. We have shown that, in addition to the condensation in the polar caps, two effects significantly contribute to the pressure cycle and lead to strong latitudinal variations of the cycle itself. The first effect is due to the large latitudinal variations of heights. The second one is purely dynamical and is linked to the strong Martian winds. Both have comparable magnitude and are stronger in high latitudes where the dy-

namical effect becomes predominant. At 75°S, the dynamical component contributes to a 25% temporal variation of the surface pressure over the course of the year, of the same magnitude as the variations due to the condensation–sublimation cycle. The two effects tend to reinforce in midlatitude and counteract each other in polar regions. Locally, longitudinal variations may amplify strongly the orographic effect. In addition to their intrinsic interest, these conclusions must be taken into account in the environmental models developed for the preparation of Martian exploration. Some future Martian projects, such as the French CNES Ballon project aboard the future Russian Mars 96 mission, may be very sensitive to such pressure variations. The evolution of the mean atmospheric pressure (thin solid curve on the top panel of Fig. 5) is the only one directly representative of the condensation–sublimation cycle. However, this curve cannot be used as a reference, since the simulated pressure does not fit the Viking data closely enough. The natural continuation of this work is to tune the most uncertain parameters (the mean dust optical depth and the emissivity and albedo of CO_2 ice) in order to obtain a better fit. This is now being done and will be included in a forthcoming paper. The simulated annual evolution of the surface pressure may then be used as a database either for spatial missions or for the study of the atmospheric mass budget.

Acknowledgments. The thermal inertia and albedo maps where provided to us by Terry Martin and the Martian orography by Philippe Masson. The Viking pressure measurements were produced by Tillman (Tillman and W. 1987; Tillman 1988) and provided to us by Steven Lee and are available in digital form through the Planetary Data System. For information on ordering the dataset(s) or related documentation, contact the PDS Planetary Atmospheres Discipline Node (303-492-5348; email—Internet: lee@syrtis.colorado.edu, SPAN: ORION::LEE; Steven Lee, Laboratory for Atmospheric and Space Physics, University of Colorado, Boulder, CO 80309) or the PDS Central Node (818-306-6026; email—SPAN: JPLPDS::PDS_OPERATOR; PDS Operator, Jet Propulsion Laboratory, MS 525-3610, 4800 Oak Grove Drive, Pasadena, CA 91109). Part of the computational means were provided by the scientific committee of Centre de Calcul Vectoriel pour la Recherche. We are also grateful to Robert Sadourny for useful discussions.

REFERENCES

Fouquart, Y., and B. Bonnel, 1980: Computations of solar heating of the Earth's atmosphere: A new parametrization. *Contrib. Atmos. Phys.*, **53**, 35–62.

Haberle, R. M., C. B. Leovy, and J. B. Pollack, 1982: Some effects of global dust storms on the atmospheric circulation of Mars. *Icarus*, **50**, 322–367.

——, J. B. Pollack, J. R. Barnes, R. W. Zurek, C. B. Leovy, J. R. Murphy, H. Lee, and J. Schaeffer, 1993: Mars atmospheric dynamics as simulated by the NASA/Ames general circulation model I. the zonal-mean circulation. *JGR-Planets*, **98**(E2), 3093–3124.

Hess, S. L., R. H. Henry, and J. E. Tillman, 1979: The seasonal variation of atmospheric pressure on Mars as affected by the south polar cap. *J. Geophys. Res.*, **84**(B6), 2923–2927.

——, J. A. Ryan, J. E. Tillman, R. M. Henry, and C. B. Leovy, 1980: The annual cycle of pressure on Mars measured by *Viking* Landers *1* and *2*. *Geophys. Res. Lett.*, **7**, 197–200.

Holton, J. R., 1979: p. 101–118 *An Introduction to Dynamic Meteorology, Int. Geophys. Ser.*, Vol. 23. Academic Press, 2d ed.

Hourdin, F., 1992: A new representation of the CO_2 15 μm band for a Martian general circulation model. *J. Geophys. Res.*, **97**(E11), 18 319–18 335.

Jacobsen, I., and E. Heise, 1982: A new economical method for the computation of the surface temperature in numerical models. *Contrib. Atmos. Phys.*, **55**, 128–141.

James, P. B., G. Briggs, J. Barnes, and A. Spruck, 1979: Seasonal recession of Mars' south polar cap as seen by Viking. *J. Geophys. Res.*, **84**(B6), 2889–2922.

Leighton, R. R., and B. C. Murray, 1966: Behavior of carbon dioxide and other volatiles on Mars. *Science*, **153**, 136–144.

Leovy, C. B., 1979: Martian meteorology. *Ann. Rev. Astron. Astrophys.*, **17**, 387–413.

Magalhaes, J. A., 1987: The Martian Hadley circulation: Comparison of "viscous" predictions to observations. *Icarus*, **70**, 442–468.

Martin, T. Z., 1986: Thermal infrared opacity of the Mars atmosphere. *Icarus*, **66**, 2–21.

Mellor, G. L., and T. Yamada, 1974: A hierarchy of turbulence closure models for planetary boundary layers. *J. Atmos. Sci.*, **31**, 1791–1806.

Morcrette, J. J., L. Smith, and Y. Fouquart, 1986: Pressure and temperature dependence of the absorption in longwave radiation parametrizations. *Contrib. Atmos. Phys.*, **59**(4), 455–469.

Paige, D. A., and A. P. Ingersoll, 1985: Annual heat balance of Martian polar caps: Viking observations. *Science*, **228**, 1160–1168.

Pollack, J. B., D. S. Colburn, F. M. Flasar, R. Kahn, C. E. Carlston, and D. Pidek, 1979: Properties and effects of dust particles suspended in the Martian atmosphere. *J. Geophys. Res.*, **84**(B6), 2929–2945.

——, C. B. Leowy, P. W. Greiman, and Y. Mintz, 1981: A Martian General Circulation Model experiment with large topography. *J. Atmos. Sci.*, **38**, 3–29.

——, R. M. Haberle, J. Schaeffer, and H. Lee, 1990: Simulations of the general circulation of the Martian atmosphere I: Polar processes. *J. Geophys. Res.*, **95**, 1447–1473.

——, ——, J. R. Murphy, J. Shaeffer, and H. Lee, 1993: Simulation of the general circulation of the Martian atmosphere II: seasonnal pressure variations. *JGR-Planets*, **98**(E2), 3149–3181.

Sadourny, R., 1975: The dynamics of finite-difference models of the shallow-water equations. *J. Atmos. Sci.*, **32**, 680–689.

——, and K. Laval, 1984: January and July performance of the LMD general circulation model. *New Perspectives in Climate Modeling*, A. Berger and C. Nicolis, Eds., Elsevier, 173–197.

Talagrand, O., F. Hourdin, and F. Forget, 1991: The LMD Martian general circulation model: Results about the annual pressure cycle. *BAAS*, **23**, 1217. [Oral presentation at the 23d annual DPS meeting (Palo Alto, California).]

Tillman, J. E., 1988: Mars global atmospheric oscillations: Annually synchronized transient normal-mode oscillations and the triggering of global dust storms. *J. Geophys. Res.*, **93**(D8), 9433–9451.

——, and G. W., 1987: Atmospheric pressure, point by point values. VL1 sols 1-2245 and VL2 sols 1-1050. Tech. Rep. National Space Sciences Data Center.

Warren, S. G., W. J. Wiscombe, and J. F. Firestone, 1990: Spectral albedo and emissivity of CO_2 in Martian polar caps: Model results. *J. Geophys. Res.*, **95**, 717–741.

Warrilow, D. A., A. B. Sangster, and A. Slingo, 1986: Modeling of land surface processes and their influence on European climate. Tech. Rep. DCTN 38, UKMO, Meteorological Office, London Road, Bracknell, Berkshire, United Kingdom.

Zurek, R. W., J. R. Barnes, R. M. Haberle, J. B. Pollack, J. E. Tillman, and C. B. Leovy, 1992: Dynamics of the atmosphere of Mars. *Mars*, The University of Arizona Press, 835–933.